




Revisiting the abundance pattern and charge-exchange emission in the M82 centre

K. Fukushima¹, S. B. Kobayashi¹, and K. Matsushita¹

Department of Physics, Tokyo University of Science, 1-3 Kagurazaka, Shinjuku-ku, Tokyo 162-8601, Japan
e-mail: kxfukushima@gmail.com (K.F.)

Received / Accepted

ABSTRACT

Context. The interstellar medium (ISM) in starburst galaxies contains plenty of chemical elements synthesised by core-collapse supernova explosions. By measuring the abundances of these metals, we can study the chemical enrichment within galaxies and the transportation of metals into circumgalactic environments through powerful outflows.

Aims. We perform the spectral analysis of the X-ray emissions from the M82 core using the Reflection Grating Spectrometer (RGS) onboard *XMM-Newton* to accurately estimate the metal abundances in the ISM.

Methods. We analyse over 300 ks of RGS data observed with fourteen position angles, covering an 80 arcsec cross-dispersion width. We employ multi-temperature thermal plasma components in collisional ionisation equilibrium (CIE) to reproduce the observed spectra, each exhibiting different spatial broadenings.

Results. The O VII band CCD image shows a broader distribution compared to those for O VIII and Fe-L bands. The O VIII line profiles have a prominent double-peaked structure, corresponding to the northward and southward outflows. The O VII triplet feature exhibits marginal peaks, and a single CIE component, convolved with the O VII band image, approximately reproduces the spectral shape. Combining a CIE model with a charge-exchange emission model also successfully reproduces the O VII line profiles. However, the ratio of these two components varies significantly with the observed position angles, which is physically implausible. Spectral fitting of the broadband spectra suggests a multi-temperature phase in the ISM, approximated by three components at 0.1, 0.4, and 0.7 keV. Notably, the 0.1 keV component exhibits a broader distribution than the 0.4 and 0.7 keV plasmas. The derived abundance pattern shows super-solar N/O, solar Ne/O and Mg/O, and half-solar Fe/O ratios. These results indicate the chemical enrichments by core-collapse supernovae in starburst galaxies.

Key words. astrochemistry – ISM: abundances – galaxies: individual: M82 – galaxies: ISM – galaxies: starburst – X-rays: ISM

1. Introduction

Core-collapse supernovae (CCSNe) from massive star progenitors play a crucial role in the evolution of galaxies. They are primary sources of light α -elements such as O, Ne, and Mg (e.g., Nomoto et al. 2013). Additionally, they heat the interstellar medium (ISM) to X-ray-emitting temperatures. In starburst galaxies, in particular regions of active star formation, CCSNe can induce powerful winds from the galactic disc. These winds, also known as outflows, are essential in the enrichment of the circumgalactic medium that connects the ISM to the local Universe (Orlitova 2020, for a comprehensive review). Consequently, X-ray observations of starburst galaxies offer valuable insights into the processes supplying energies and metals into both the ISM and circumgalactic spaces.

In recent years, numerous X-ray observations have focused on the extended X-ray-emitting ISM in starburst galaxies (e.g., Strickland et al. 2004; Yamasaki et al. 2009; Konami et al. 2012; Mitsuishi et al. 2013; Yang et al. 2020). The M82 galaxy, a well-established starburst system located at a 3.53 Mpc distance from our solar system ($l' \sim 1$ kpc thereat, Karachentsev et al. 2004), has been a key object among these studies. The nearly edge-on appearance makes this galaxy an ideal laboratory for studying biconical outflows that erupt from the central region of the galaxy (e.g., Strickland & Heckman 2009; Zhang 2018). These outflows exhibit a multiphase structure, which is observed in the

infrared, H α , and X-ray windows (Strickland et al. 1997; Lehnert et al. 1999; Read & Stevens 2002; Engelbracht et al. 2006; Zhang et al. 2014; Lopez et al. 2020). Strickland & Heckman (2007) found diffuse Fe He α emission in the central regions, suggesting the presence of gas at temperatures of several kiloelectronvolts. Additionally, strong emission lines of elements such as O, Mg, Si, S, and Fe have been detected from the core to the wind regions of the galaxy (e.g., Tsuru et al. 1997, 2007; Ranalli et al. 2008; Konami et al. 2011). In the central regions, these elements show an unusual abundance pattern: super-solar ratios of Ne/O and Mg/O (> 1.5 solar) with super-solar O/Fe ratios have been reported (e.g., Tsuru et al. 1997; Ranalli et al. 2008; Konami et al. 2011; Zhang et al. 2014). This contradicts the pre-existing nucleosynthesis models of CCSN (e.g., Nomoto et al. 2013). In contrast, the outflowing gas outside the disc shows an abundance pattern consistent with CCSN predictions (Tsuru et al. 2007; Konami et al. 2011).

An additional exciting feature in M82 is the presence of charge exchange (CX) X-ray emission. In this process, one or more electrons are transferred from a cold neutral atom to a hot ion. Subsequently, the cascade relaxation of such a captured electron from a highly excited energy state to the ground state of the ion result in the X-ray line emission (e.g., Cravens 2002; Sibeck et al. 2018; Gu & Shah 2023). A notable feature of the CX process is present in the O VII triplet structure: the enhanced forbidden line at 0.56 keV compared to the resonance line at 0.57

keV. In starburst galaxies, it is expected to observe CX emissions at the fronts of hot gas flows colliding with cold matter. Liu et al. (2012) analysed the data from the Reflection Grating Spectrometer (RGS) on board *XMM-Newton* and reported this enhancement in the O VII triplet in several starburst galaxies, suggesting a significant CX contribution in addition to plasma in a collisional ionisation equilibrium (CIE) state. Konami et al. (2011) and Lopez et al. (2020) included the CX component in their analysis of the CCD spectra from M82, although their spectral resolution was limited to resolve the O VII triplet sufficiently. Zhang et al. (2014) used the RGS data from an *XMM-Newton* observation of M82 and estimated that the interaction area between the neutral and ionised matter is significantly larger than the geometry surface area of the galaxy.

The RGS on board *XMM-Newton* is effective for our study, offering good spatial and spectral resolution within the ~ 0.5 – 2 keV band. This makes it particularly useful for measuring α -element abundances and estimating the CX contribution. However, any line structures in the dispersed spectra are practically broadened when the source extends $\gtrsim 0.8$ arcmin, leading to decreased resolving power for extended objects such as galaxies (Mao et al. 2023, for a recent review). Therefore, careful treatment is required when analysing the RGS spectra of galaxies, especially for the broadening effect on each emission line (e.g., Chen et al. 2018; Yang et al. 2020; Fukushima et al. 2023). In this study, we used deep 300 ks RGS data obtained with different position angles to model the spectra of the central region of M82 to determine its temperature structure, the CX contribution, and the abundance pattern. The paper is structured as follows. Section 2 summarises the *XMM-Newton* observations and data reduction. In Sect. 3, we outline the line-broadening effect intrinsic to the RGS analysis. Section 4 presents the general prescription for our fitting and the results. We will discuss and interpret our findings in Sect. 5. We assume cosmological parameters as $H_0 = 70 \text{ km s}^{-1} \text{ Mpc}^{-1}$, $\Omega_m = 0.3$, and $\Omega_\Lambda = 0.7$. The protosolar abundance of Lodders et al. (2009) is adopted to estimate element abundances.

2. Observations and data reduction

We analysed the archival observation data of the M82 centre with RGS installed on *XMM-Newton*. Table 1 summarises the observations used in this work. The M82 nucleus (Lester et al. 1990) is located near the centre of the MOS detector for these observations. The RGS data were processed using the `rgsproc` task wrapped in the *XMM-Newton* Science Analysis System (SAS) version 18.0.0. We obtained light curves from the CCD9 on the RGS focal plane (den Herder et al. 2001); and next, the mean count rate μ and standard deviation σ were derived by fitting these curves with a Gaussian. In order to discard background soft-proton flares, the count rate threshold as $\mu \pm 2\sigma$ was applied to uncleaned events. Following the SAS team, other standard screening criteria were employed. The cleaned exposure times of each observation are in Table 1.

3. Imaging analysis

In Figs. 1(a), (b), and (c), we show X-ray images of the M82 centre for the O VII (Fig. 1(a), 0.55–0.60 keV), O VIII Ly α (Fig. 1(b), 0.64–0.67 keV), and Fe-L (Fig. 1(c), 0.70–1.20 keV) bands. Avoiding relatively large noises in the O VII band image, we subtract the continuum counts from the raw events. Point-like sources are not discarded. In these images, the outflows extend-

Table 1. The RGS observations analysed in this work.

ObsID	Date	Exposure ^a (ks)	Position angle ^b (deg)
0112290201	2001 May 06	19.2	293
0206080101 ^c	2004 Apr 21	55.3	319
0560590101	2008 Oct 03	27.8	138
0560181301	2009 Apr 03	22.9	316
0560590201	2009 Apr 17	15.1	316
0560590301	2009 Apr 29	21.4	296
0657800101	2011 Mar 18	22.8	330
0657801701	2011 Apr 11	21.4	312
0657801901	2011 Apr 29	11.6	296
0657802101	2011 Sep 24	12.4	147
0657802301	2011 Nov 21	9.2	100
0870940101	2021 Apr 06	28.6	313
0891060101	2021 Oct 17	26.8	127
0891060401	2022 Apr 06	32.1	313

Notes. ^(a) Half the sum of the RGS1 and RGS2 exposures after the deflaring procedure. ^(b) The angle of the RGS dispersion axis measured eastwards from the celestial north. ^(c) The data set analysed in Zhang et al. (2014).

ing from the disc towards the southeast and northwest are visible, especially in Figs. 1(a) and (b). The dispersion directions for the three representative position angles are overlaid. The 80 arcsec cross-dispersion width covers a significant part of the two outflow regions. Incorporating data from different position angles helps resolve the degeneracy between energy and spatial position along the dispersion angle, allowing for a more detailed analysis of the outflow structure.

The X-ray count profiles within an 80 arcsec cross-dispersion width along each dispersion axes are given in Figs. 1(d), (e), and (f). These profiles show significant differences across the three bandpasses. In particular, the Fe-L line band is characterised by a centrally peaked and narrow distribution on a spatial scale of 1–2 arcmin. In contrast, the O VII band exhibits the most broadened profiles. In both the O VII and O VIII profiles, a dip is observed at ~ 1 arcmin offset northward from the galaxy centre. The two peaks beside the dip correspond to the outflows towards the southeast and northeast. This bimodal line profile in the O band, along the centrally-peaked distribution in the Fe-L line band, has been reported by Zhang et al. (2014). The appearances of this double-peak structure, especially in the O VIII band profile, depends on the dispersion direction (Figs. 1(d) and (f)).

4. Spectral analysis

4.1. General prescription

The RGS spectra along the dispersion direction can be used within a 5 arcmin cross-dispersion width centred on the MOS detector (e.g., Zhang et al. 2019; Narita et al. 2023). After filtering the cleaned event files with XDSP_CORR columns using `evselect`, we extracted first-order RGS spectra from the 80 arcsec cross-dispersion width centred on the M82 nucleus by the `rgsspectrum` task. This method takes advantage of determining accurately the rectangular cross-dispersion limits¹ compared to the standard RGS analysis with `xpsf`-options of

¹ Alternatively, one can use the `rgsregions` task to do this if specifying a rectangle that is roughly symmetrical about the detector centre.

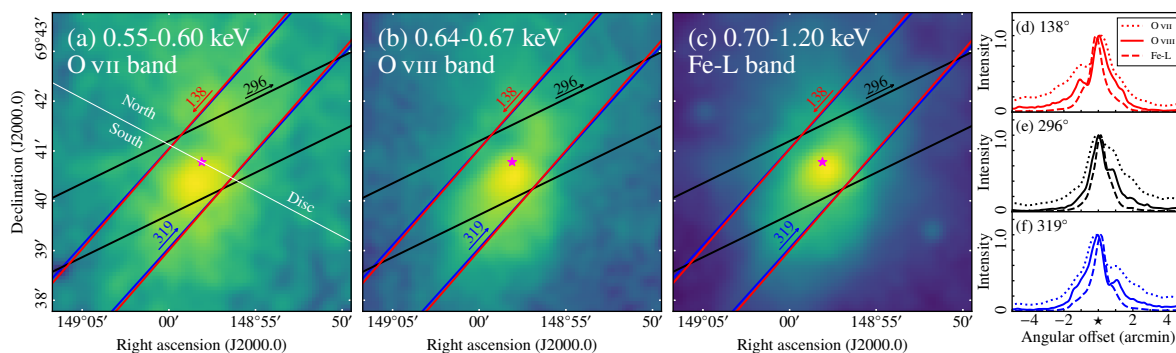


Fig. 1. (a) Mosaiced X-ray count image of the M82 centre in the O VII (0.55–0.60 keV) band by CCDs. The representative three RGS position angles are overlaid with the 80 arcsec cross-dispersion widths. The arrows indicate each dispersion direction in which the photons are scattered into the higher energy side. The star marker and the solid line passing through it indicate the M82 centre and disc (Lester et al. 1990; Mayya et al. 2005). The continuum flux estimated using the 0.45–0.55 keV band is subtracted from the raw count image. (b, c) Same as (a), but in the O VIII Ly α (0.64–0.67 keV) and Fe-L (0.70–1.20 keV) bands. (d) Normalized count profiles projected on to the 138° dispersion axis in the 0.55–0.60 keV (O VII), 0.64–0.67 keV (O VIII), and 0.70–1.20 keV (dominated by Fe-L lines) bands. The angular offset is measured in reference to the star marker in (a), where the positive side of the offset axis is the higher energy part in diffracted spectra. (e, f) Same as (d), but along the dispersion axes of 296° and 319°, respectively.

rgsproc, for instance (e.g., Fukushima et al. 2022, 2023). The cross-dispersion widths and dispersion directions for three representative position angles are plotted in Figs. 1(a), (b), and (c). The RGS1 and RGS2 spectra and response matrices are co-added through the rgscombine script.

The RGS instrument is primarily designed for observing point-like sources; therefore, the response matrices generated by the standard sas method are unsuitable for analysing diffuse emissions from various extended sources, such as supernova remnants, galaxies, and clusters (e.g., Chen et al. 2018; Tateishi et al. 2021; Fukushima et al. 2023). Line broadening in a first-order RGS spectrum is observed as $\Delta E = 0.138\Delta\theta$, where ΔE and $\Delta\theta$ represent the line broadening and the spatial extent in the wavelength (Å) and dispersion (arcmin) axes, respectively. To fit the RGS spectra of these extended sources, it is necessary to convolve the response matrix with the projected surface-brightness profile along the dispersion direction (e.g., Tamura & Ohta 2004; Mao et al. 2023). Moreover, variations in spatial broadening across different energy bands necessitate applying different convolution scales for distinct spectral components. The differences in the spatial distribution of the O VII, O VIII, and Fe-L band images (Section 3) imply the presence of multiple thermal CIE components with different spatial scales. Zhang et al. (2014) carefully analysed the RGS spectra of M82, adopting two spectral broadenings: bimodal soft emission and centrally-peaked hard emission. In the subsequent part, we further test different spatial broadenings for the spectra components emitting O VII and O VIII lines.

We use the xSPEC package version 12.10.1f (Arnaud 1996) but with the revised AtomDB version 3.0.9 (Smith et al. 2001; Foster et al. 2012) that provides information on the line and continuum emissions at two hundred and one temperatures from 8.6×10^{-4} to 86 keV. This updated AtomDB is implemented standardly in xSPEC version 12.11.0k or later². The C-statistic method (Cash 1979) is adopted in our spectral fitting to estimate the spectral parameters and the error ranges thereof without bias (Kaastra 2017). Each spectrum is re-binned to have a minimum of 1 count per spectral bin.

Otherwise, users are strongly urged to check the generated RMFs and effective areas.

² <http://www.atomdb.org>

4.2. Spectral models

In our RGS spectral analysis, we will reproduce the diffuse ISM emission (denoted by ISM_{M82}). Two individual absorptions modify the ISM_{M82} component. We assume $6.7 \times 10^{20} \text{ cm}^{-2}$ for the Galactic extinction (Willingale et al. 2013). The intrinsic absorption of M82 for diffuse emissions is typically $(1-3) \times 10^{21} \text{ cm}^{-2}$ (e.g., Konami et al. 2011; Zhang et al. 2014); thus, we use the fixed value $2 \times 10^{21} \text{ cm}^{-2}$. The photoelectric absorption cross-sections are retrieved from Verner et al. (1996). Letting these absorption parameters free does not significantly change the results we demonstrate below. We do not include diffuse astrophysical background emissions such as the cosmic X-ray background or Milky Way halo component in our spectral fitting since they contribute to the observed RGS spectra just as flat components. A power-law component is introduced to account for increasing flux at low energies below 0.5 keV. We use another power-law component with a 1.6 photon index (Ranalli et al. 2008) subjected to $2 \times 10^{22} \text{ cm}^{-2}$ extinction to take the point source emission into account.

The complete model applied to the observed spectra is represented as $\text{phabs}_{\text{Gal}} \times (\text{phabs}_{\text{M82}} \times \text{ISM}_{\text{M82}} + \text{phabs}_{\text{PS}} \times \text{powerlaw}_{\text{PS}}) + \text{powerlaw}_{\text{BKG}}$. To account for the line broadening effect on ISM_{M82} described in Sects. 1 and 3, we use the xSPEC model rgsxsrc with mosaiced CCD (MOS+pn) images in specific bands. We first perform spectral fits in two local bands: the O VIII band (0.60–0.77 keV, Sect. 4.3) and O VII band (0.45–0.62 keV, Sect. 4.4), each convolved with the respective images. Then, we fit the broadband spectra covering the full RGS energy range of 0.45–1.75 keV (hereafter broadband; Sect. 4.5), using the image of this band, which closely resembles the Fe-L band image. The spatial distribution of each emission line may not precisely match the image of its corresponding energy band, as these bands also include continuum emissions. The image convolution approach in this study is an approximation, as well as similar works, and the resulting systematic uncertainties will be discussed in further sections.

4.3. Results of O VIII Ly α line

First, we test the thermal plasma component in collisional ionisation equilibrium (CIE) convolved with the O VIII band image:

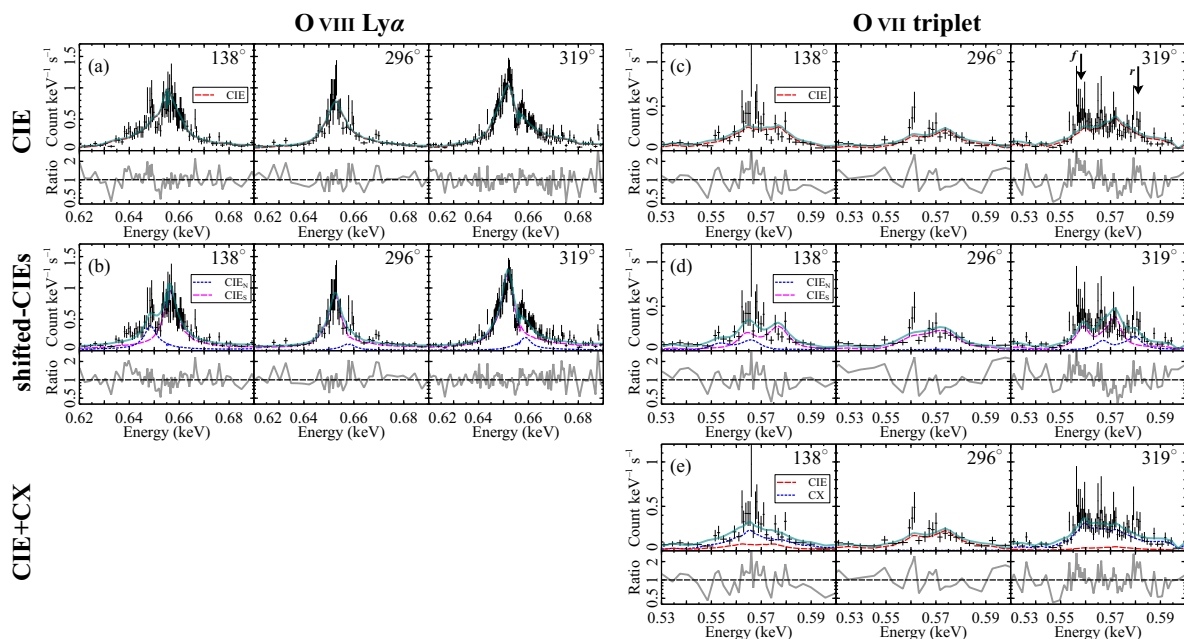


Fig. 2. The RGS spectra of the M82 centre in the O VIII (a, b) and O VII (c, d, e) bands for the three representative position angles. The best-fitting models and the data-to-model ratios for the three methods are plotted: the CIE modelling convolved with local band images (the first row), the shifted-CIEs modelling convolved by the broadband image (the second row), and the CIE+CX modelling convolved with the O VII band image (the third row, only for the O VII lines). The positions of the O VII forbidden and resonance lines are labelled in the 319° panel of (c).

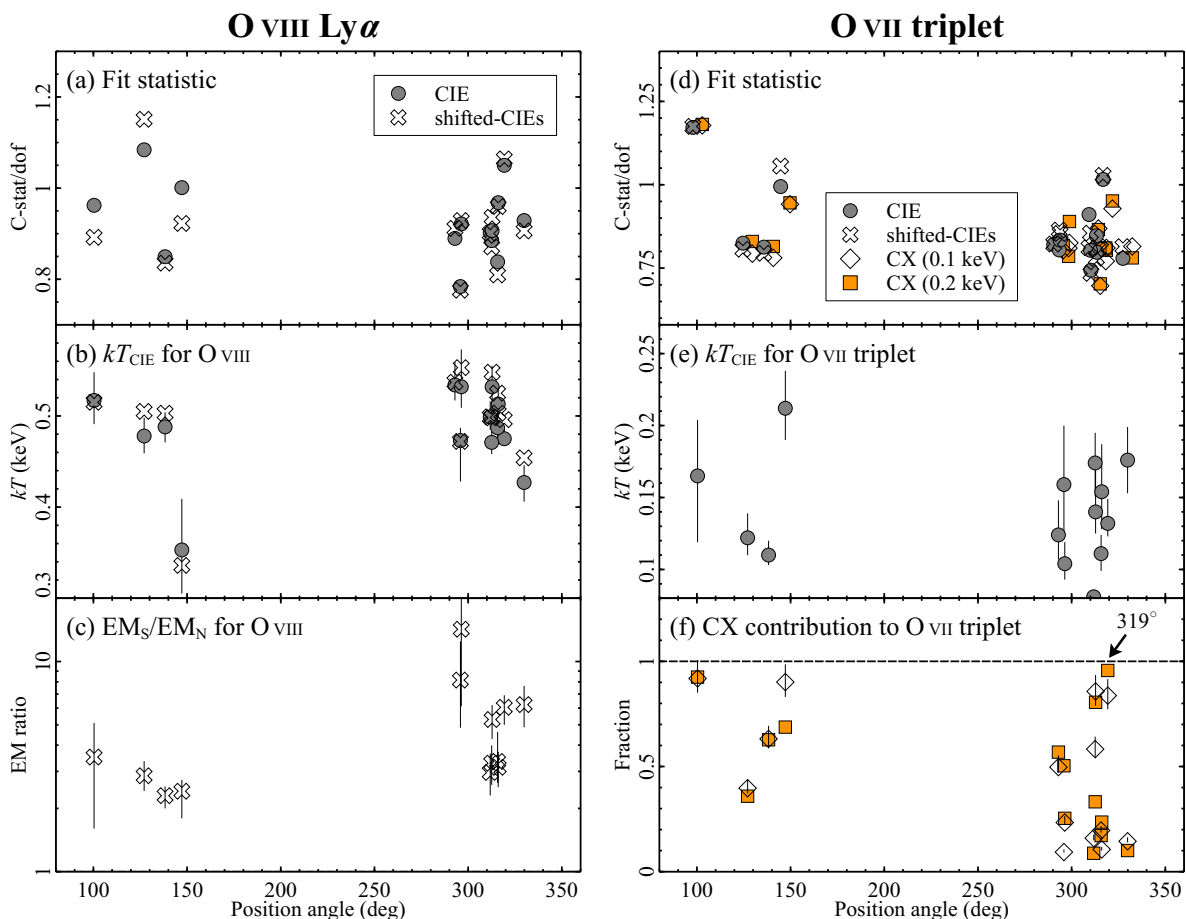


Fig. 3. (a) C-stats/dof values from the CIE and shifted-CIEs modellings on the 0.60–0.77 keV band (O VIII and Fe XVII) plotted against the RGS position angle. (b) Temperatures derived from the two modellings. (c) The EM_S/EM_N profile obtained from the shifted-CIEs method. (d) Same as (a), but on the 0.45–0.62 keV band fitting (N VII and O VII). The results are from the CIE, shifted-CIEs (0.14 keV), and CIE+CX modellings. (e) Temperatures derived from the CIE modelling. (f) Flux contribution of CX components to the O VII line.

$ISM_{M82} = \text{vapec}$ (the CIE modelling). We ignore the point source contribution due to quite a strong intrinsic absorption for the point sources at the M82 centre ($\gtrsim 1 \times 10^{22} \text{ cm}^{-2}$, e.g., [Brightman et al. 2016](#)). Despite focusing on local line structures, in the spectral fittings, we use a wider energy range of 0.60–0.77 keV, including the Fe xvii line around 0.73 keV. This approach enabled more robust measurement of global parameters such as kT ; restricting to “local fits” lead to poorly constrained values (e.g., [Lakhchaura et al. 2019](#)). The combined spectrum of each observation is fitted with free parameters of kT , emission measure (EM), and the O and Fe abundances.

The CIE modelling approximately reproduces the observed spectra (Fig. 2(a)), achieving good C-statistics/dof values $\lesssim 1.2$ (the x -axes of Fig. 3(a)). However, a spectral sub-peak corresponding to the northward wind region at ~ 0.65 keV and ~ 0.66 keV for the position angle of 138° and 319° , respectively, appears narrower than the spectral model convolved with the O viii band image. The derived kT_{CIE} values are plotted against the RGS position angle in Fig. 3(b), yielding a uniform kT_{CIE} with a median of 0.49 keV and a 16–84th percentile range of 0.47–0.53 keV.

Figure 3 shows that the O viii Ly α consists of a main peak and sub peak ~ 5 eV away from it, whose intensities depend on the RGS dispersion direction. The 5 eV separation between the two peaks at ~ 0.66 keV corresponds to an angular diameter of 1 arcmin along the dispersion direction (Fig. 1(b)). To reproduce this double-peak structure, we then try two spatially distinct components with varying redshift parameters to represent different spatial positions: $ISM_{M82} = \text{vapec}_N + \text{vapec}_S$ (the shifted-CIEs modelling). Here, subscripts “N” and “S” represent the northeast and southwest emission peaks, respectively. The temperature and metal abundances of the two components are assumed to have the same values. Each CIE component is convolved with the broadband image (0.45–1.75 keV) as the extent of each peak is similar to that of the Fe-L band (Figs. 1(d), (e), and (f)). While our subscript nomenclature is not an *a priori* assumption, it describes the observed spectral features, including the sub-peak structure for the northward wind (Fig. 2(b)). Good C-stat/dof values are derived on the O viii line (Fig. 3(a)). This model yields similar temperatures with the CIE modelling (Fig. 3(b)). The EM_S/EM_N ratios are greater than unity for all position angles (Fig. 3(c)): the brighter vapec_S is shifted to the harder side and the softer side when the dispersion angle is inverted (Fig. 2(b)). This variation naturally arises due to minor differences among RGS slices. Thus, our shifted-CIEs method approximates successfully and reasonably the spatial variation and broadening of the O viii Ly α line; that is, the double CIE modelling with the broadband image can be a surrogate for an actual emission plasma broadened as the O viii band image.

4.4. Results of O vii triplet lines

For the O vii triplet feature, we also start with the CIE modelling with the O vii band image: $ISM_{M82} = \text{vapec}$. The ignorance of the point-source contribution aligns with Sect. 4.3. On the same philosophy of the O viii Ly α band analysis, we utilise the 0.45–0.62 keV band, including the N vii line at 0.5 keV. The spectra are fitted with free parameters of kT , emission measure (EM), and the N and O abundances. As shown in Fig. 2(c), the best-fit CIE models, convolved with the O vii band image, closely resemble the observed line profile of O vii. We obtain good C-stat/dof for all dispersions (the x -axes of Fig. 3(d)). A hint of residuals is seen at the forbidden line energy of 0.56 keV, although their significance is relatively tiny. For example, in the 319° angle,

which exhibits the largest residual, it remains at $\sim 3\sigma$. The CIE modelling for O vii provides a uniform kT_{CIE} across the position angles as does the O viii band one (Fig. 3(e)). The median value and 16–84th percentile range for kT_{CIE} are 0.14 keV and 0.11–0.18 keV, respectively.

Next, we apply the shifted-CIEs modelling for O vii taking into account its marginal bimodality: $ISM_{M82} = \text{vapec}_N + \text{vapec}_S$. Each CIE component is convolved with the broad RGS bandpass (0.45–1.75 keV). Considering the relatively widespread O vii profile (Figs. 1(d), (e), and (f)), the additional broadening option of the *APEC* model is adopted. We set the temperature of the two CIE components to $kT = 0.14$ keV based on the results of the CIE modelling. This model effectively fits the broadened O vii lines (Figs. 2(d)), yielding C-stat/dof values similar to those from the CIE modellings (Fig. 3(d)). The significance of the residuals at 0.56 keV decreased to a maximum of 2σ . For certain datasets, including that for the position angle of 296° , a single CIE component is sufficient to represent the spectra, where the dominant component likely corresponds to the bright southwest outflow.

The hint of residuals at 0.56 keV might be attributable to the CX emission. To constrain the contribution of the CX component, we employ the second version of the AtomDB CX Model *acx* ([Smith et al. 2014](#)), together with a CIE plasma: $ISM_{M82} = \text{vapec} + \text{vacx}$ (the CIE+CX modelling). Both components are convolved in this model with the O vii band image. The collision velocity between ions and atoms is set to moderate values 200 km s^{-1} (e.g., [Cumbee et al. 2016](#); [Zhang 2018](#)). We assumed that the CIE and CX components share the same temperature (and abundance), testing two temperature assumptions of $kT = 0.1$ and 0.2 keV. The CIE+CX model also gives fine-fits for all spectra under both temperature assumptions (Figs. 2(e) and 3(d)). However, this CIE+CX modelling still resulted in similar residuals around the forbidden line at a level of $\sim 2\sigma$ at most. Additionally, Fig. 3(g) shows that at certain position angles, the CX emission significantly exceeds the CIE contribution, reaching up to 96 per cent at 319° , *AND VICE VERSA*. There is no clear correlation between the CX fraction and position angle; for example, similar angles yield significantly different CX fractions. The lack of a consistent pattern leads to the conclusion that the CIE+CX models may not be physically plausible.

The minor residuals observed at 0.56 keV correspond to the energy of the forbidden line of O vii for the bright southward wind component. We attempted to introduce a spatially narrower CX component to fill the residuals. We modified the CIE+CX model by replacing the broader CX component with a more localised and less broadened one. This modified model does not change our results nor improve spectral fits, making it challenging to assert the robust presence of the CX emission based on the current RGS data. [Okon et al. \(2024\)](#) recently discussed a possible localised CX emission. However, they introduce a different model in which the low-energy side of the observed spectrum is attributed predominantly to the CX emission.

4.5. Results of broadband spectra

Finally, we fit the broadband RGS spectra (0.45–1.75 keV), excluding the CX model from this analysis. Our adopted model is $ISM_{M82} = \text{vapec}_{\text{hot}} + \text{vapec}_{\text{warmN}} + \text{vapec}_{\text{warmS}} + \text{vapec}_{\text{coolN}} + \text{vapec}_{\text{coolS}}$. All of the CIE components are convolved with the broadband image. As described in Sects. 4.3 and 4.4, two CIEs for the cool and warm plasma, when convolved with the broadband image, effectively reproduce the local band spectra. These gas components mainly contribute to the O vii and O viii lines,

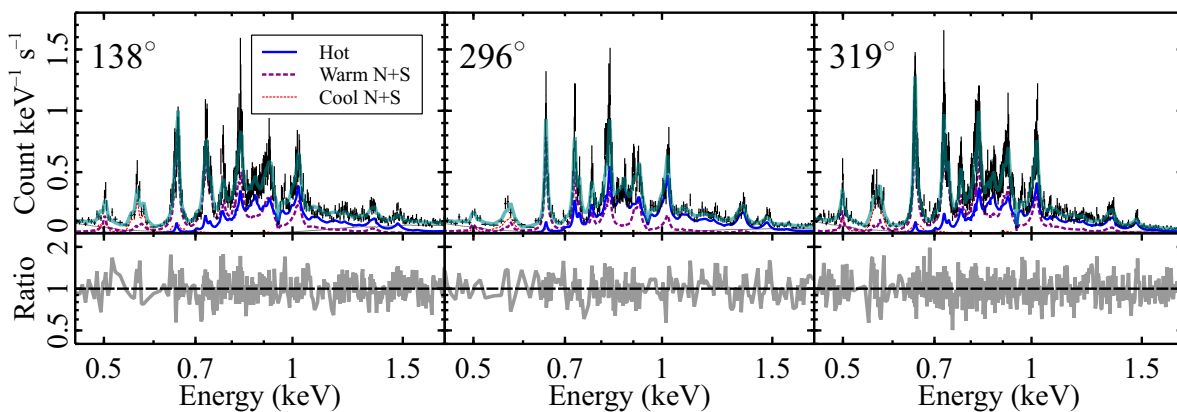


Fig. 4. The best-fitting models to the broadband RGS spectra of the M82 centre for the three position angles. Thin dotted and solid lines represent the background and point-source components, respectively (see Sect. 4.1).

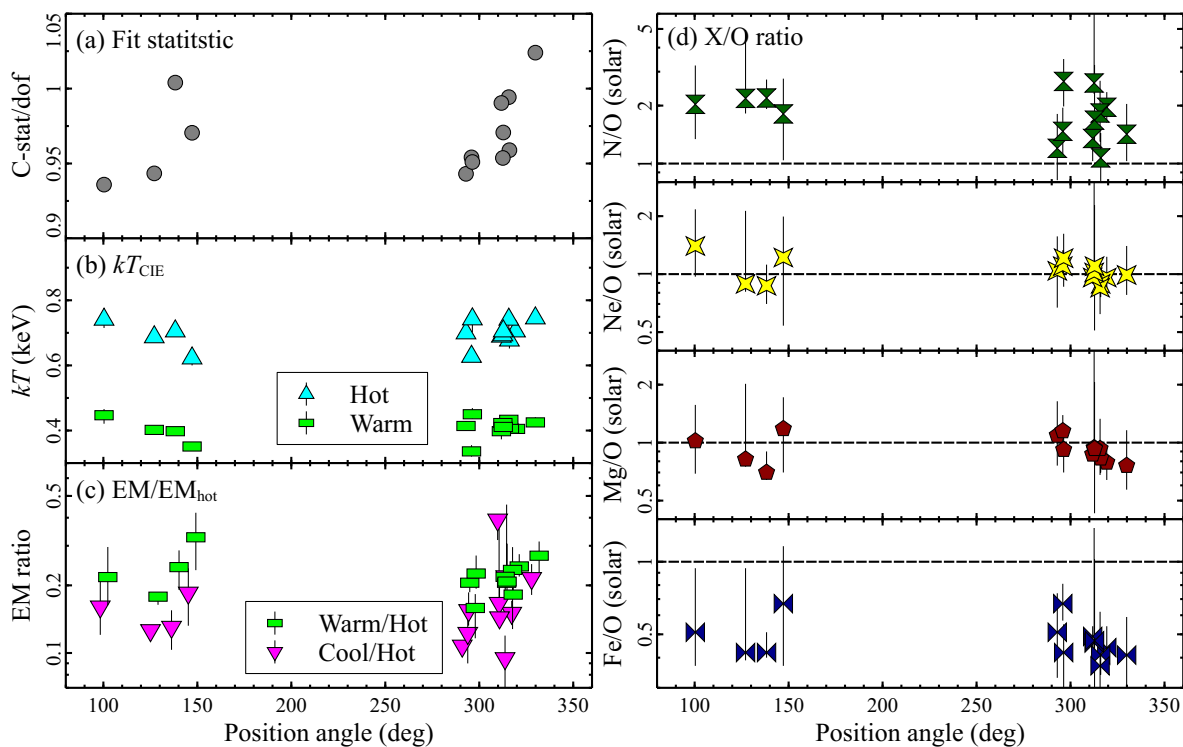


Fig. 5. (a) C-stat/dof values from the the 0.45–1.75 keV band fitting plotted against the RGS position angle. (b) Temperatures of the warm and hot components. (c) Relative EM/EM_{hot} ratios for the cool and warm plasmas. (d) Abundance ratios of N/O (vertical ties), Ne/O (ninja-stars), Mg/O (pentagons), and Fe/O (horizontal ties).

with the new hot component mainly accounting for the Fe-L and Mg lines. In this model, kT_{hot} , kT_{warm} and EMs of each component are varied freely, under the assumption that $kT_{\text{warmN}} = kT_{\text{warmS}}$. We fix kT_{cool} to 0.14 keV. The N, O, Ne, Mg, Fe, and Ni abundances are free parameters with shared values across all spectral components, and other metals are set to 1 solar. Unfortunately, firm constraints on the Ni abundance are not very promising since clear Ni line structures are rarely detected by RGS, even in highly metal-rich systems (e.g., the Centaurus cluster, Sanders et al. 2008; Fukushima et al. 2022). The intrinsic absorption for the hot plasma in M82, which is more substantial than for the warm and cool gases (see Sect. 4.1), is difficult to constrain. Hence, we adopt $8 \times 10^{21} \text{ cm}^{-2}$ for the hot component extinction, consistent with the intrinsic absorption estimated for the hot gases by the CCD study ($kT \gtrsim 0.7 \text{ keV}$, Lopez et al. 2020). Other prescriptions for the warm and cool components follow the ones

with each shifted-CIEs modelling (Sects. 4.3 and 4.4). Despite a bit simplistic modelling, the mean values of the cool+warm and hot gas absorptions are close to fixed values when allowed to vary.

The best-fitting models for the representative broadband spectra of M82 are shown in Fig. 4. As we designed, each CIE component contributes to observed emission lines. This model yields good fits with excellent C-stat/dof values up to 1.1 for all observations (Fig. 5(a)). In Fig. 5(b), we plot the derived kT_{hot} and kT_{warm} against the position angles. We obtain the medians and 16–84th percentile ranges as $kT_{\text{hot}} = 0.70$ (0.68–0.74) keV and $kT_{\text{warm}} = 0.41$ (0.40–0.43) keV. The inclusion of the hot gas in the Fe-L lines results in a slight decrease in the kT_{warm} value compared to the results from the shifted-CIEs method for the local O VIII band. Figure 5(c) reveals uniform values for the relative EMs of each temperature plasma. Here, the hot component is

more dominant than the other two, with the warm and cool gases in similar intensities. The abundance ratios, N/O, Ne/O, Mg/O, and Fe/O, are also uniform across the dataset: super-solar N/O, solar ratios of Ne/O and Mg/O, and sub-solar Fe/O (Fig. 5(d)). The Ni values are not plotted due to large errors and scatters as warned above. In particular, the solar abundance ratios of light α -elements near the disc are the first report, which will be discussed more in detail in Sect. 5.3.

5. Discussion

5.1. Multi-temperature phase in the M82 centre

In our analysis of the RGS spectra from multiple position angles, we determined that the hot (0.7 keV), warm (0.4 keV), and cool (0.1–0.2 keV) components effectively represent the temperature structure of the ISM in M82. The 0.6–0.7 keV component, responsible for Mg (and possibly Si) emission lines, was also reported in studies using RGS and CCD data [Read & Stevens 2002](#); [Origlia et al. 2004](#); [Konami et al. 2011](#); [Zhang et al. 2014](#); [Lopez et al. 2020](#)). A warm plasma component with $kT \sim 0.5$ keV has also been identified by [Ranalli et al. \(2008\)](#). The presence of another cool gas contribution was predicted through line diagnostics of the O VII triplet, suggesting $kT \sim 0.1$ – 0.3 keV, [Ranalli et al. 2008](#)). However, such a cool component at the M82 core has not been reported (e.g., [Zhang et al. 2014](#); [Lopez et al. 2020](#)), except for a hint of the 0.2 keV component ([Konami et al. 2011](#), but CCD study). The O VII emission has often been interpreted as a result of the CX processes (e.g., [Zhang et al. 2014](#)). However, in our spectral model, which accounts for different spatial broadenings for O VII and O VIII, the CIE components are the primary contributors to these line emissions.

Observational and simulation studies generally predict the core regions of starburst galaxies undergo a multi-temperature phase of gas, ranging from cold dust to hot outflows (e.g., [Leroy et al. 2015](#)). Interestingly, such a multiphase state is also applicable to X-ray-emitting gas itself (e.g., [Melioli et al. 2013](#); [Schneider et al. 2018](#)). This theoretical prediction is in good agreement with the plasma content that we revealed for M82, as well as with other starburst galaxies (e.g., NGC 3079, [Konami et al. 2012](#); Arp 299, [Mao et al. 2021](#)). Furthermore, even in the Milky Way, certain regions with a high concentration of massive stars, such as superbubbles, possess intermixed X-ray plasma with different temperatures (e.g., [Kim et al. 2017](#) for simulation; [Fuller et al. 2023](#) for observation). The multiphase ISM would be ubiquitous in star-forming regions, regardless of their scale. While the origin of different spatial variations of the cool and warm components eludes our present study, we expect it to be examined more robustly through the high-resolution observation of M82.

5.2. Note of CX emission

Previous reports on the CX emission from M82 did focus on the limited position angle (mainly the 319° observation, [Liu et al. 2011](#); [Zhang et al. 2014](#)). In this angle, the O VII profile expands toward the low energy scale (Figs. 1(d) and (f)). This expansion is interpreted as high R- or G-ratio values³ in the energy space. The enhancement in the soft part of the O VII triplet is likely due to the bright outflow towards the southeast, as discussed in Sect. 4.4. While our current results do not strongly favour CX

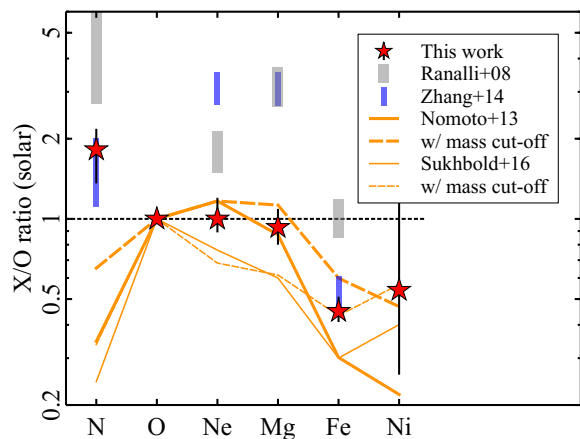


Fig. 6. Observed X/O abundance pattern from the broadband spectral fits, where the medians and 16–84th percentile ranges for all dispersion angles are plotted. Two literal values by previous RGS works are given for comparison. The dashed line represents the solar composition. The thick and thin solid lines indicate the IMF-weighted yields predicted by [Nomoto et al. \(2013\)](#) and [Sukhbold et al. \(2016\)](#), respectively, assuming the solar initial metallicity for progenitors. The dashed lines are for each option of the mass-cut-off integration ($< 25 M_\odot$).

emissions, we consider its contribution in M82 using the 319° result that is the most significantly contaminated by the CX emission if any. We assume that the CX and CIE components share the same spatial distribution, although a more localised CX emission can be debated (Sect. 4.4). From this observation, we obtained an ACX normalisation of $(3.3 \pm 1.0) \times 10^{-4} \text{ cm}^{-5}$. According to the study of M51 by [Yang et al. \(2020\)](#), we can evaluate the spatial scale of the CX reaction from this ACX normalisation as

$$\frac{10^{-10}}{4\pi D^2} \int \frac{n}{\sigma} dA. \quad (1)$$

Here, D , n , and σ are the angular diameter distance to M82, the density of receiver ions in the CX reaction and the CX cross sections, respectively. Assuming a spherical volume with a 40 arcsec (~ 0.67 kpc at M82) radius, we adopted $n = 0.19 \text{ cm}^{-3}$ from the CIE modelling in Sect. 4.4. The cross sections were set as $\sigma = 5 \times 10^{-15} \text{ cm}^2$ ([Gu & Shah 2023](#), and references therein). In consequence, we obtained the CX emitting area $A = 14 \pm 3 \text{ kpc}^2$. Similar illustrations are reported by [Zhang et al. \(2014\)](#) for the same M82 centre and [Yang et al. \(2020\)](#) for M51. This significant discrepancy makes us suspicious about the brightness of the CX emission if the broadened CX component is a dominant source of the O VII triplet lines. Indeed, [Okon et al. \(2024\)](#) propose that the CX component accounts for 40–60 per cent of the O VII flux using a multi-temperature model, substantially lower than the previous estimate (~ 90 per cent, [Zhang et al. 2014](#)). The CX emission properties in M82, such as luminosity or spatial extent, must be under continuous vigilance to be challenged or validated more confidently with the high-resolution and non-dispersive X-ray spectroscopic data coming down from *XRISM* in orbit.

5.3. Metal abundance pattern

The metal abundance pattern is a key to studying the chemical enrichment process of observed gases. Figure 6 shows the median values and the 16–84th percentile ranges of N/O, Ne/O, Mg/O, and Fe/O across all position angles. For comparison, we also plot the Ni/O value, which is in possible agreement with

³ These ratios are given as f/i (R) and $(i+f)/r$ (G), where r , f , and i are the flux of resonance, forbidden, and intercombination lines, respectively

Fe/O within a large error. We obtained solar-like ratios of the Ne/O and Mg/O that are lower than the results of two earlier RGS works (Ranalli et al. 2008; Zhang et al. 2014). Other studies with CCD reported super-solar patterns of light α -elements (e.g., Konami et al. 2011). The presence or absence of the CX contribution does not change the super-solar abundances in these studies. The primary origin of these gaps would be our careful modelling of the O VII and O VIII lines rather than the presence of CX emission, which improves the estimation of a temperature structure in M82. In particular, the inclusion of the cool gas component would be essential progress in measuring the element abundances.

In Fig 6, we compare the observed abundance pattern in the M82 centre, a starburst system, with nucleosynthesis models of CCSNe. This comparison is crucial as most supernovae in such systems are expected to originate from massive stars. We adopt two models: the “classical” standard yield by Nomoto et al. (2013) and the latest N20 calculations by Sukhbold et al. (2016). For both models, we assume an initial mass function (IMF) by Salpeter (1955) with progenitor masses up to $40 M_{\odot}$. In addition, based on the discussion on the missing progenitor mass problem for CCSNe by Smartt (2015), we also employ another IMF-weighted integration with the upper mass limit of $25 M_{\odot}$.

For α -elements, the yields with Nomoto et al. (2013) most closely match the observed Ne/O and Mg/O ratios but tend to underestimate the Fe/O and Ni/O ones. For the case with the upper mass limit of $25 M_{\odot}$, the half-solar Fe/O and Ni/O values are explained well by both of Nomoto et al. (2013) and Sukhbold et al. (2016). In a powerful starburst galaxy Arp 299, Mao et al. (2021) provide a similar picture by comparing the model yields to the N/O, Ne/O, Mg/O, S/O, and Ni/O pattern. However, the observed Fe/O and Ni/O ratios in M82 might also be explained by including a minor contribution from Type Ia SNe (only 6 per cent of the total SNe in the M82 core). The hot ISM in M82, as in other starburst galaxies, serves as a significant repository of CCSN products.

None of these CCSNe models adequately reproduce the N/O ratio ~ 2 solar in M82. Similar high N/O ratios have been reported in more ancient systems, such as early-type galaxies, including the brightest cluster galaxies (e.g., Mao et al. 2019; Fukushima et al. 2023). These objects owe a dominant fraction of their N enrichment to mass-loss winds from massive and asymptotic giant branch stars. Thus, such mass-loss channels, aside from CCSNe, likely contribute to the enrichment observed in the core of M82. One caveat is that the N VII Ly α line is present at ~ 0.5 keV and is likely to be affected by, for example, the estimation of the absorption for the cool+ warm component and/or the contribution of the background emission (Sect. 4). When the gate valve is opened, the X $RISM$ data will provide us a great opportunity to constrain the N abundance more robustly.

Acknowledgements. The authors would like to thank Dr. D. Wang for taking the time to read our manuscript thoroughly as a reviewer and for providing helpful comments and suggestions. K.F. shall deem it an honour to be supported by the Japan Society for the Promotion of Science (JSPS) through Grants-in-Aid for Scientific Research (KAKENHI) grant Nos. 21J21541 and 22KJ2797 (Grant-in-Aid for JSPS Fellows). This work is based on observations obtained with XMM-Newton, an ESA science mission with instruments and contributions directly funded by ESA Member States and NASA of the USA. The XMM-Newton Science Archive (<https://nxsas.esac.esa.int/nxsas-web/>) stores and distributes the RGS data analysed in this paper. We get the second version of ACX from the AromDB website (<http://www.atomdb.org/CX/>) and run it on the PYXSPEC module implemented in the XSPEC package. The figures in this paper are generated using VEUSZ (<https://veusz.github.io>) and PYTHON (<https://www.python.org>).

References

- Arnaud, K. A. 1996, in *Astronomical Society of the Pacific Conference Series*, Vol. 101, *Astronomical Data Analysis Software and Systems V*, ed. G. H. Jacoby & J. Barnes, 17
- Brightman, M., Harrison, F. A., Barret, D., et al. 2016, *ApJ*, 829, 28
- Cash, W. 1979, *ApJ*, 228, 939
- Chen, Y., Wang, Q. D., Zhang, G.-Y., Zhang, S., & Ji, L. 2018, *ApJ*, 861, 138
- Cravens, T. E. 2002, *Science*, 296, 1042
- Cumbee, R. S., Liu, L., Lyons, D., et al. 2016, *MNRAS*, 458, 3554
- den Herder, J. W., Brinkman, A. C., Kahn, S. M., et al. 2001, *A&A*, 365, L7
- Engelbracht, C. W., Kundurthy, P., Gordon, K. D., et al. 2006, *ApJ*, 642, L127
- Foster, A. R., Ji, L., Smith, R. K., & Brickhouse, N. S. 2012, *ApJ*, 756, 128
- Fukushima, K., Kobayashi, S. B., & Matsushita, K. 2022, *MNRAS*, 514, 4222
- Fukushima, K., Kobayashi, S. B., & Matsushita, K. 2023, *ApJ*, 953, 112
- Fuller, C. A., Kaaret, P., Bluem, J., et al. 2023, *ApJ*, 943, 61
- Gu, L. & Shah, C. 2023, in *High-Resolution X-ray Spectroscopy: Instrumentation, Data Analysis, and Science*, ed. C. Bambi & J. Jiang (Springer Nature Singapore), 255–289
- Kaastra, J. S. 2017, *A&A*, 605, A51
- Karachentsev, I. D., Karachentseva, V. E., Huchtmeier, W. K., & Makarov, D. I. 2004, *AJ*, 127, 2031
- Kim, C.-G., Ostriker, E. C., & Raileanu, R. 2017, *ApJ*, 834, 25
- Konami, S., Matsushita, K., Gandhi, P., & Tamagawa, T. 2012, *PASJ*, 64, 117
- Konami, S., Matsushita, K., Tsuru, T. G., Gandhi, P., & Tamagawa, T. 2011, *PASJ*, 63, S913
- Lakhchaura, K., Mernier, F., & Werner, N. 2019, *A&A*, 623, A17
- Lehnert, M. D., Heckman, T. M., & Weaver, K. A. 1999, *ApJ*, 523, 575
- Leroy, A. K., Walter, F., Martini, P., et al. 2015, *ApJ*, 814, 83
- Lester, D. F., Carr, J. S., Joy, M., & Gaffney, N. 1990, *ApJ*, 352, 544
- Liu, J., Mao, S., & Wang, Q. D. 2011, *MNRAS*, 415, L64
- Liu, J., Wang, Q. D., & Mao, S. 2012, *MNRAS*, 420, 3389
- Lodders, K., Palme, H., & Gail, H. P. 2009, in *Astronomy, Astrophysics, and Cosmology*, ed. J. Trümper (Springer Berlin, Heidelberg), 560–598
- Lopez, L. A., Mathur, S., Nguyen, D. D., Thompson, T. A., & Olivier, G. M. 2020, *ApJ*, 904, 152
- Mao, J., de Plaa, J., Kaastra, J. S., et al. 2019, *A&A*, 621, A9
- Mao, J., Paerels, F., Guainazzi, M., & Kaastra, J. S. 2023, in *High-Resolution X-ray Spectroscopy: Instrumentation, Data Analysis, and Science*, ed. C. Bambi & J. Jiang (Springer Nature Singapore), 9–45
- Mao, J., Zhou, P., Simionescu, A., et al. 2021, *ApJ*, 918, L17
- Mayya, Y. D., Carrasco, L., & Luna, A. 2005, *ApJ*, 628, L33
- Melioli, C., de Gouveia Dal Pino, E. M., & Gerassate, F. G. 2013, *MNRAS*, 430, 3235
- Mitsuishi, I., Yamasaki, N. Y., & Takei, Y. 2013, *PASJ*, 65, 44
- Narita, T., Uchida, H., Yoshida, T., Tanaka, T., & Tsuru, T. G. 2023, *ApJ*, 950, 137
- Nomoto, K., Kobayashi, C., & Tominaga, N. 2013, *ARA&A*, 51, 457
- Okon, H., Smith, R. K., Picquenot, A., & Foster, A. R. 2024, *ApJ*, 963, 147
- Origlia, L., Ranalli, P., Comastri, A., & Maiolino, R. 2004, *ApJ*, 606, 862
- Orlitova, I. 2020, in *Reviews in Frontiers of Modern Astrophysics*, ed. P. Kabath, D. Jones, & M. Skarka (Springer Cham), 379–411
- Ranalli, P., Comastri, A., Origlia, L., & Maiolino, R. 2008, *MNRAS*, 386, 1464
- Read, A. M. & Stevens, I. R. 2002, *MNRAS*, 335, L36
- Salpeter, E. E. 1955, *ApJ*, 121, 161
- Sanders, J. S., Fabian, A. C., Allen, S. W., et al. 2008, *MNRAS*, 385, 1186
- Schneider, E. E., Robertson, B. E., & Thompson, T. A. 2018, *ApJ*, 862, 56
- Sibeck, D. G., Allen, R., Aryan, H., et al. 2018, *Space Sci. Rev.*, 214, 79
- Smartt, S. J. 2015, *PASA*, 32, e016
- Smith, R. K., Brickhouse, N. S., Liedahl, D. A., & Raymond, J. C. 2001, *ApJ*, 556, L91
- Smith, R. K., Foster, A. R., Edgar, R. J., & Brickhouse, N. S. 2014, *ApJ*, 787, 77
- Strickland, D. K. & Heckman, T. M. 2007, *ApJ*, 658, 258
- Strickland, D. K. & Heckman, T. M. 2009, *ApJ*, 697, 2030
- Strickland, D. K., Heckman, T. M., Colbert, E. J. M., Hoopes, C. G., & Weaver, K. A. 2004, *ApJS*, 151, 193
- Strickland, D. K., Ponman, T. J., & Stevens, I. R. 1997, *A&A*, 320, 378
- Sukhbold, T., Ertl, T., Woosley, S. E., Brown, J. M., & Janka, H. T. 2016, *ApJ*, 821, 38
- Tamura, N. & Ohta, K. 2004, *MNRAS*, 355, 617
- Tateishi, D., Katsuda, S., Terada, Y., et al. 2021, *ApJ*, 923, 187
- Tsuru, T. G., Awaki, H., Koyama, K., & Ptak, A. 1997, *PASJ*, 49, 619
- Tsuru, T. G., Ozawa, M., Hyodo, Y., et al. 2007, *PASJ*, 59, 269
- Verner, D. A., Ferland, G. J., Korista, K. T., & Yakovlev, D. G. 1996, *ApJ*, 465, 487
- Willingale, R., Starling, R. L. C., Beardmore, A. P., Tanvir, N. R., & O’Brien, P. T. 2013, *MNRAS*, 431, 394
- Yamasaki, N. Y., Sato, K., Mitsuishi, I., & Ohashi, T. 2009, *PASJ*, 61, S291
- Yang, H., Zhang, S., & Ji, L. 2020, *ApJ*, 894, 22
- Zhang, D. 2018, *Galaxies*, 6, 114
- Zhang, S., Wang, Q. D., Foster, A. R., et al. 2019, *ApJ*, 885, 157
- Zhang, S., Wang, Q. D., Ji, L., et al. 2014, *ApJ*, 794, 61